International Journal of Refrigeration 167 (2024) 246–256

Contents lists available at ScienceDirect

International Journal of Refrigeration

journal homepage: www.elsevier.com/locate/ijrefrig

1D models of an active magnetic regeneration cycle for cryogenic applications

Modèles 1D d'un cycle de régénération magnétique active pour des applications cryogéniques

Theodoros Diamantopoulos *, Tommaso Matteuzzi, Rasmus Bjørk

Department of Energy Conversion and Storage, Technical University of Denmark, Anker Engelundsvej, DK-2800 Kgs. Lyngby, Denmark

ARTICLE INFO

Keywords:
Active magnetic regenerator (AMR)
Magnetic refrigeration
Hydrogen liquefaction
Cryogenics
AMR modeling
Mean field theory

Mots clés:
Régénérateur Magnétique Actif (AMR)
Réfrigération Magnétique
Liquéfaction de l'Hydrogène
Cryogénie
Modélisation AMR
Théorie du Champ Moléculaire

ABSTRACT

In investigation of an active magnetic regenerator (AMR) cycle operating at room temperatures, 1D models have been extensively used to accurately computing its performance metrics. However, extending these models to simulate an AMR cycle at cryogenic temperatures introduces inherent complexities and challenges. The broad temperature span and low operating temperatures required for cryogenic applications, such as hydrogen liquefaction, lead to significant density variations of the working fluid within the AMR that cannot be overlooked. In this work, two 1D AMR models assuming a compressible working fluid operating at cryogenic temperatures are demonstrated which address the large density variations and the numerical stiffness of the equations. The models exhibit good agreement with experimental and 2D numerical results of an AMR configuration designed for hydrogen liquefaction. A comparative study is conducted between the developed models and an incompressible AMR model at cryogenic temperatures shows that the incompressible model predicts cooling powers that are higher by a factor of up to 10 at high values of utilization, highlighting the error of assuming an incompressible fluid on estimating the performance metrics.

1. Introduction

For the wider adoption of hydrogen as a viable alternative to fossil fuels, its liquefaction is the main driver that necessitates optimization and minimization of its overall cost (Restelli et al., 2024). Commonly used refrigeration technologies for liquefying hydrogen (LH_2), such as the Linde–Hampson, Claude, and Collins cycles, are widely used in industrial applications due to their established methodologies and reliability (Ghorbani et al., 2023). However, these processes are notably energy-intensive, with specific energy consumption (SEC) ranging approximately from 10.8 to 13.8 kWh/kgLH_2 (Ghorbani et al., 2023; Zhang et al., 2023a). Although there is some SEC improvement via the use of mixed refrigerants, the latter poses questions regarding their environmental impact, especially once these technologies scale up. Furthermore, even with current improvements, these refrigeration technologies are far from meeting the efficiency targets set by entities such as the US Department of Energy, which aims for a SEC of 6 kWh/kgLH_2 (Zhang et al., 2023a). This gap between theoretical and commercial efficiency highlights a significant area for improvement. Current large-scale liquefaction plants, even those with advanced designs (SEC of ~8 kWh/kgLH_2), struggle with inefficiencies and high operational expenditures (OPEX), further emphasizing the need for technological advancements in this field. Furthermore, small-scale existing liquefaction plants suffer from higher SEC (>12 kWh/kgLH_2) and their adoption is restricted because of higher capital expenditures (CAPEX).

In the pursuit of enhanced hydrogen liquefaction efficiency and economic viability, recent research has focused on the application of magnetic refrigeration (MR) technologies. Active Magnetic Regeneration (AMR) stands as a pivotal refrigeration technology that employs magnetocaloric materials (MCMs), an externally applied magnetic field, and a working fluid to drive a Brayton-like refrigeration cycle (Kitanovski et al., 2016; Kitanovski, 2020; Gómez et al., 2013). MCMs are magnetic materials that exhibit a change in temperature when subjected to an external magnetic field (Smith et al., 2012). This temperature change of the MCM can be amplified by employing a working fluid via a regenerative process in the active magnetic regeneration cycle.

* Corresponding author.
E-mail address: thedi@dtu.dk (T. Diamantopoulos).

https://doi.org/10.1016/j.ijrefrig.2024.08.011
Received 12 March 2024; Received in revised form 21 June 2024; Accepted 13 August 2024
Available online 20 August 2024
0140-7007/© 2024 The Authors. Published by Elsevier B.V. This is an open access article under the CC BY license (http://creativecommons.org/licenses/by/4.0/).

AMR offers several advantages over conventional liquefaction technologies. AMR is not only competitive in terms of energy consumption and exergy efficiency (Ansarinasab et al., 2023) but also a more cost-effective and manageable solution with its inherently simpler design (Zhang et al., 2023a). Furthermore, AMR can be utilized as a pre-cooling stage (Ansarinasab et al., 2023) or an intermediate stage (Kamiya et al., 2022; Park and Jeong, 2017; Adapa et al., 2024) within a refrigeration cycle, enhancing the theoretical efficiency and reducing the SEC of the liquefaction cycle. Most importantly, MR reduces the environmental impact associated with mixed refrigerant liquefaction cycles, making them a more sustainable option for large-scale hydrogen production.

Traditionally, the AMR process has been applied in room-temperature magnetic refrigeration (Eriksen et al., 2015, 2016; Gottschall et al., 2018; Waske et al., 2018; Capovilla et al., 2016). However, recent attention in the field has moved towards cryogenic temperatures (Numazawa et al., 2014; Barclay et al., 2019; Taskaev et al., 2020; Archipley et al., 2022; Teyber et al., 2019; Tang et al., 2022; Zhang et al., 2023b; Liu et al., 2024). For instance, a recent study demonstrated the AMR's capability to liquefy small amounts of hydrogen, marking a significant stride in the green transition (Kamiya et al., 2022). Nevertheless, to ensure efficient AMR devices for hydrogen liquefaction, optimization is essential, which necessitates accurate models that specifically capture the underlying physics of AMR devices, especially in the cryogenic temperature range.

A common approach to modeling active magnetic regenerator (AMR) devices is the use of 1D models. These models allow for easier exploration of the parameter space due to their computational speed, thereby facilitating the identification of optimal configurations and operating ranges for the targeted AMR device. In the room temperature range, various 1D models have been formulated for AMR devices in different applications (Silva et al., 2021; Nakashima et al., 2022). Most models assume non-thermal equilibrium between the magnetocaloric material (MCM) and the working fluid (Engelbrecht, 2008; Matsumoto et al., 2011; Park et al., 2015), although models that assume local thermal equilibrium have also been developed (Rowe, 2012).

At room operating temperatures, the commonly used working fluid is an incompressible fluid, most often water (Eriksen et al., 2015, 2016). This choice significantly simplifies the modeling of the AMR device. Firstly, the continuity equation for the mass conservation of the fluid is inherently satisfied. Secondly, the momentum equation is simplified as the balance between the pressure gradient and the adopted drag force model. Therefore, the AMR model condenses into coupled time-dependent thermal energy equations of the working fluid and the solid matrix (Lei et al., 2017).

However, at cryogenic temperatures, such as in hydrogen liquefaction within a temperature range approximately from liquid nitrogen temperature of 77 K to hydrogen liquefaction at 20 K, i.e., a temperature span of $\Delta T_s = 57\,\mathrm{K}$ across the AMR, a compressible gas such as helium is often utilized (Park and Jeong, 2017). The choice of helium as the working fluid in conjunction with cryogenic temperatures fundamentally alters the required modeling approach. This is illustrated by the observation that within this temperature range, under constant operational pressure across the regenerator, the density of the helium working fluid undergoes a four-fold increase from the hot to the cold end as it is shown in Fig. 1. Such a large density difference will eventually drive non-uniform velocity fields across the regenerator which will affect the overall temperature distribution of the regenerator and thus the calculated overall performance metrics of the modeled device. Hence, to accurately compute these metrics the spatiotemporal evolution of all the fluid field variables needs to be captured by the model. Consequently, one has to adhere to solving the fully non-linear compressible equations which describe the fluid motion and energetics within the porous MCM.

The cryogenic AMR device model involves forced convection of an oscillating compressible fluid in a porous medium. In this context, the unsteady flow necessitates accounting for time-dependent equations. Additionally, as previously stated, operating at cryogenic temperatures introduces significant density changes in the working fluid, precluding the use of approximations such as according to Boussinesq (Kundu et al., 2015). Lastly, the flow within a porous medium indicates that the fluid flow velocities are small in magnitude compared to its speed of sound, i.e., low Mach number flow $\mathcal{O}(<10^{-2})$, which introduces stiffness when numerically integrating the compressible Navier–Stokes equations in time.

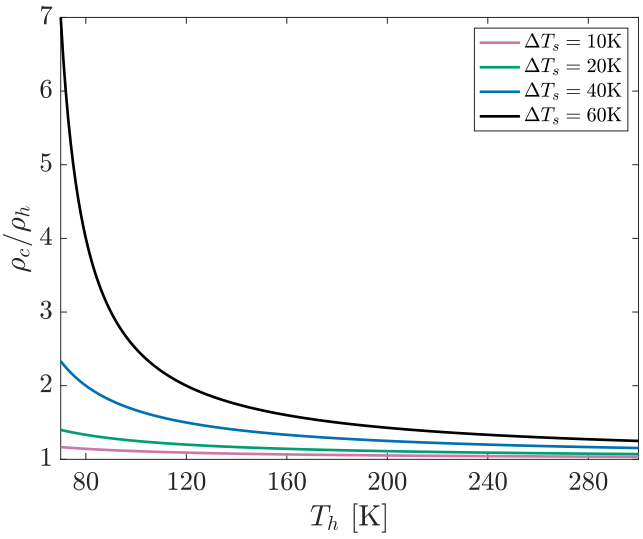

Fig. 1. Ratio of the density of the fluid at the cold, ρ_c, and hot, ρ_h, reservoirs of an ideal gas at constant pressure as a function of the hot reservoir temperature T_h, for different temperature spans ΔT_s. The range of values of T_h span from cryogenic, encountered in hydrogen liquefaction, to room temperature applications (Bell et al., 2014).

While 2D AMR models for hydrogen liquefaction, which consider the compressibility and unsteadiness of the flow, have previously been utilized (Zheng et al., 2023), their application is limited due to extensive computational costs. Therefore, for exploring the parameter space in designing AMR devices at cryogenic temperatures, 1D AMR models remain the most computationally efficient approach. Although 1D AMR models have been used to simulate hydrogen liquefaction (Smaïli et al., 2011; Feng et al., 2020), they either do not account for the full unsteadiness of the fluid variables (i.e., velocity) or assume a constant reference density throughout the AMR cycle. For room temperature operation the latter assumption is justified and validated against experimental results (Burdyny and Rowe, 2013); however, at cryogenic temperature ranges, the density difference of the fluid among the regenerator is more substantial, as discussed earlier. Consequently, this density variation has to be taken into account by the numerical AMR model.

This work introduces two 1D AMR models using a compressible working fluid, which solve the volume-averaged compressible Navier–Stokes equations. These models extend the AMR model initially developed by Engelbrecht (2008), Lei et al. (2017) to cryogenic temperature ranges, and they inherently consider flow unsteadiness and large density variations. The arising stiffness is addressed by either adopting an implicit-explicit (IMEX) time integration scheme (Boscheri and Pareschi, 2021) or a pressure-correction scheme (Knikker, 2011) of the asymptotically expanded compressible Navier–Stokes equations for low-Mach number (LMN) flows (Müller, 1998).

The paper's structure is as follows: Section 2 delineates the governing equations, Section 3 details the two models, their discretization, and the implementation of the cycle's boundary conditions. Section 4 presents how metrics, which assess the performance and cyclic-convergence, are computed. Validation against previously published

experimental and numerical results is conducted in Section 5. Section 6 compares the performance metrics for a cryogenic test-case between the developed compressible solver and the incompressible solver by Engelbrecht (2008). Finally, concluding remarks are provided in Section 7.

2. Governing equations of the AMR

The equations that describe the flow of a compressible fluid within the solid matrix, i.e., regenerator, are the compressible Navier–Stokes equations under the Darcy–Forchheimer equation. The compressible Navier–Stokes equations for a flow within a porous medium are derived through a volume-averaged approach. For more details regarding the volume-averaged compressible Navier–Stokes equations and their derivation, the reader is referred to the work of Li et al. (2020), Mößner and Radespiel (2015), Jarauta et al. (2020). The continuity equation in conservative form, which describes the conservation of mass of the working fluid within the regenerator, is given by Bejan (2013)

$$\frac{\partial(\varepsilon\rho_f)}{\partial t} + \nabla\cdot\left(\rho_f \boldsymbol{u}\right) = 0 \tag{1}$$

where ρ_f is the density of the fluid, ε is the porosity, and $\boldsymbol{u}$ is the superficial or Darcy velocity (Nield et al., 2006). This velocity is the volume-average velocity computed within a volume that includes both the solid and fluid phases. In general, fluid properties are denoted with the subscript f, while s denotes the properties of the solid. Note that all the fluid flow field variables along with the solid temperature are intrinsic volume-averaged quantities. Regarding the conservation of the fluid's momentum, under the assumption of a Darcian fluid flow, the viscous stresses within the momentum and consequently their contribution in the energy equation are omitted (Costa, 2006). Thus, the momentum equation within the porous region, expressed through the superficial velocity and under the assumption of uniform porosity throughout the solid matrix, is given by Teng and Zhao (2000), Rochette and Clain (2005), Nield (2007)

$$\frac{1}{\varepsilon}\frac{\partial(\rho_f \boldsymbol{u})}{\partial t} + \frac{1}{\varepsilon^2}\nabla\cdot\left(\rho_f \boldsymbol{u}\otimes\boldsymbol{u}\right) = -\nabla p - \boldsymbol{F_d} \tag{2}$$

where the convective term is shown here for completeness, but is not taken into account within the numerical model (Nield et al., 2006; Trevizoli and Barbosa, 2017; Liu and Vasilyev, 2007). $\boldsymbol{F_d}$ denotes the drag force exerted by the solid porous medium on the fluid (Barletta, 2015; Mößner and Radespiel, 2015). Note that various correlations can be used depending on the geometry of the solid matrix to approximate the overall effect of the drag force (Lei et al., 2017). For the purposes of this study $\boldsymbol{F_d}$ is computed under the Darcy–Forchheimer relation for a packed bed filled with spheres of uniform diameter,

$$\boldsymbol{F_d} = \frac{\mu}{K}\boldsymbol{u} + \frac{c_f\rho_f}{\sqrt{K}}|\boldsymbol{u}|\boldsymbol{u} \tag{3}$$

where $K = \varepsilon^3 d_p^2/180(1-\varepsilon)^2$ is the permeability, $c_f = 1.8/\sqrt{180}\varepsilon^{3/2}$ is a dimensionless drag constant (Nield et al., 2006), both derived to satisfy Ergun's relation under the Darcy–Forchheimer relation (Kaviany, 2012; Macdonald et al., 1979). Lastly, d_p is the uniform diameter of the spheres within the packed bed. Notice the absolute value of the velocity in the quadratic term, since the flow within the context of an AMR device is not unidirectional but oscillates during an AMR cycle (Nield et al., 2006). It is a common practice for the nonlinear Forchheimer term to be included in the porous medium model for flows with $Re > 10$ (Nield et al., 2006) which are encountered in the operational range of AMR applications (Lei et al., 2017; Engelbrecht, 2008; Trevizoli and Barbosa, 2017). The pressure $p = p(x,t)$ in the momentum equation is the sum of the spatially uniform reference pressure $p_0(t)$ (Paolucci, 1982) and a pressure perturbation $p_1(\boldsymbol{x},t)$, i.e., $p(\boldsymbol{x},t) = p_0(t) + p_1(\boldsymbol{x},t)$. The uniform pressure p_0 is already known and set by the operational parameters of the device. Now, the total energy equation for a compressible fluid in conservative form (Li et al., 2020) is given by

$$\varepsilon\frac{\partial\left(\rho_f E\right)}{\partial t} + \nabla\cdot\left(\boldsymbol{u}\rho_f h\right) + \frac{1}{\varepsilon^2}\nabla\cdot\left(\boldsymbol{u}\rho_f\frac{u^2}{2}\right) = \nabla\cdot\left(k_f^{\text{eff}}\nabla T_f\right) - h_c a_s\left(T_f - T_s\right) \tag{4}$$

where E is the total energy of the fluid, i.e., the sum of the internal and kinetic energy, h is the enthalpy of the fluid, k_f^{eff} is the effective thermal conductivity of the fluid due to axial dispersion, h_c is the heat transfer coefficient, a_s is the specific surface area, and T_f, T_s are the temperatures of the fluid and solid, respectively. Notice that the pressure work term (Bird et al., 2002) encountered in the case of compressible fluid flow is included through the enthalpy flux term of the total energy equation, and for the case of an incompressible fluid, this would have been omitted via the solenoidal velocity field.

The thermal equation of the fluid used in the context of a low-Mach number flow, i.e., following an asymptotic expansion with respect to the Mach number (Ma), and subsequently volume-averaged to accommodate for a porous media flow, is Nield (2007):

$$\rho_f c_p\left(\varepsilon\frac{\partial T_f}{\partial t} + \boldsymbol{u}\cdot\nabla T_f\right) = \nabla\cdot\left(k_f^{\text{eff}}\nabla T_f\right) - h_c a_s\left(T_f - T_s\right) + \boldsymbol{F_d}\cdot\boldsymbol{u} + \varepsilon\frac{\partial p_0}{\partial t} \tag{5}$$

where the second to last term on the left-hand side is the viscous dissipation. In this work p_0 is a constant, and thus its temporal derivative is zero. Lastly, the thermal equation for the solid magnetocaloric material is the same as the one used in incompressible 1D AMR models (Engelbrecht, 2008) and is given by

$$(1-\varepsilon)\rho_s\left(c_H\frac{\partial T_s}{\partial t} + T_s\left(\frac{\partial s_s}{\partial H}\right)_{T_s}\frac{\partial H}{\partial t}\right) = \nabla\cdot\left(k_s^{\text{eff}}\nabla T_s\right) + h_c a_s\left(T_f - T_s\right) \tag{6}$$

where ρ_s is the density of the solid, c_H is the specific heat capacity of the MCM, s_s is the specific entropy, k_s^{eff} is the axial effective thermal conductivity of the solid and H is the applied magnetic field, which can be modified to include demagnetization effects. The inclusion of irreversibilities due to hysteresis is omitted since this study only considers second-order materials. In both the energy equations of the two phases, the heat conduction term, as well as the convection term, emerge from closure of the volume-averaged equations (Kaviany, 2012; DeGroot and Straatman, 2011).

Regarding the fluid flow correlations, the effective thermal conductivity of the fluid for a porous medium filled with spherical particles can be found in Engelbrecht (2008), Kaviany (2012). For the solid, the effective static thermal conductivity k_s^{eff} is calculated using the correlations given by Hadley (1986). The Nusselt number correlation for a packed sphere bed porous medium, from which the heat transfer coefficient h_c is computed, can be found in Lei et al. (2017). Other correlations used in 1D AMR modeling studies for various geometries of the solid matrix including a packed-bed can be found in Lei et al. (2017).

3. Discretization of the two models

Given the significantly low velocities of the working fluid within the porous medium compared to its speed of sound, indicating a low-Mach number flow, a considerable challenge arises regarding the numerical stability of the developed solver. Firstly, for such small velocities encountered within a packed bed, the pressure evolves very rapidly, introducing stiffness to the discretized equations. Secondly, due to the large temperature gradient across the regenerator, one cannot adhere to widely used stiffly-stable schemes for incompressible flows such as those discussed in Kim and Moin (1985), since the density variations of the fluid can be substantial, as discussed previously. Consequently, two approaches are followed to address the above challenges. One is based

on a stiffly-stable IMEX scheme for the compressible Navier–Stokes equations, developed by Boscheri and Pareschi (2021), which solves a pressure wave equation derived through the total energy equation of the fluid. The second approach is a pressure-correction scheme based on the asymptotic expansion of the compressible Navier–Stokes equations for low Mach number flows described in Knikker (2011).

3.1. Time integration of the IMEX scheme

The IMEX scheme is broken down into three consecutive parts: (1) the explicit integration of the continuity equation, (2) the implicit solve of a pressure-based equation, and (3) the explicit integration of the momentum equation using the newly computed pressure. This study is the first time a stiffly-stable IMEX scheme is used for simulating compressible flow within an active magnetic regeneration cycle. The goal of the AMR model is to approximate the steady-state behavior of the AMR cycle and derive useful design insights; thus, using the most accurate time discretization for the explicit parts of the IMEX scheme is not a priority.

The explicit Euler method is used for the semi-discretization of Eq. (1) as

$$\varepsilon \frac{\rho_f^{n+1} - \rho_f^n}{\Delta t} + \nabla \cdot \left(\rho_f \boldsymbol{u}\right)^n = 0 \tag{7}$$

where $n+1$ and n are the indexes which correspond to the values of the new and the previous time-step respectively.

Similarly, the momentum equation is discretized in time. At this point of the IMEX scheme the $\left(\rho_f u\right)^{n+1}$ term is given as a function of the pressure gradient term ∇p^{n+1} at the new time-step as

$$\frac{1}{\varepsilon} \frac{\left(\rho_f \boldsymbol{u}\right)^{n+1} - \left(\rho_f \boldsymbol{u}\right)^n}{\Delta t} = -\nabla p^{n+1} - \boldsymbol{F}_{\boldsymbol{d}}^n \tag{8}$$

By expressing the kinetic energy of the total energy E^{n+1} and the enthalpy flux in a semi-implicit discretization the semi-discrete total energy equation takes the following form

$$\begin{aligned} &\frac{\varepsilon}{\Delta t}\left(\left(\rho_f e\right)^{n+1} + \frac{\left(\rho_f \mathbf{u}\right)^n}{2\varepsilon^2 \rho_f^n} \cdot \left(\rho_f \mathbf{u}\right)^{n+1} - (\rho E)^n\right) + \nabla \cdot \left(h\left(\rho_f \mathbf{u}\right)^{n+1}\right) \\ &+ \frac{1}{\varepsilon^2} \nabla \cdot \left(\boldsymbol{u} \rho_f \frac{u^2}{2}\right)^n \\ &= \nabla \cdot \left(k_f^{\mathrm{eff}} \nabla T_f^{n+1}\right) - h_c a_s \left(T_f^{n+1} - T_s^{n+1}\right) \end{aligned} \tag{9}$$

where $\rho_f e = p/(\gamma - 1)$ and $T_f = p/(R\rho_f)$ are obtained from the equation of state (EOS) for an ideal gas, with e being the specific internal energy, γ the specific heat capacity ratio, and R is the gas constant. Note that the pressure in the EOS in the IMEX scheme is the total pressure, i.e., the sum of the constant reference and spatially variable pressure. The thermophysical properties of the working fluid, namely the specific heat capacity ratio γ, viscosity μ, and thermal conductivity k_f, are functions of temperature and pressure and are evaluated using CoolProp (Bell et al., 2014). At each timestep, these properties are computed for the pressure and temperature of the fluid, which are equal to those at the previous timestep. Then, by combining the EOS and Eq. (8), the elliptic equation for the pressure is derived as

$$\begin{aligned} &\left(\frac{1}{\gamma - 1} + \frac{\Delta t}{\varepsilon} \frac{h_c a_s}{R\rho_f^{n+1}}\right) p^{n+1} - \Delta t \frac{\left(\rho_f \boldsymbol{u}\right)^n}{2\varepsilon \rho_f^n} \cdot \nabla p^{n+1} - \Delta t^2 \nabla \cdot \left(h^n \nabla p^{n+1}\right) \\ &- \frac{\Delta t}{\varepsilon} \nabla \cdot \left(k_f^{\mathrm{eff}} \nabla \left(\frac{p}{R\rho_f}\right)^{n+1}\right) - \frac{\Delta t}{\varepsilon} h_c a_s T_s^{n+1} = \\ &\left(\rho_f E\right)^* - \frac{\left(\rho_f \boldsymbol{u}\right)^n}{2\varepsilon^2 \rho_f^n} \left(\rho_f \boldsymbol{u}\right)^* - \frac{\Delta t}{\varepsilon} \nabla \cdot \left(h^n \left(\rho_f \boldsymbol{u}\right)^*\right) \end{aligned} \tag{10}$$

where h stands for the specific enthalpy. Lastly, the $\left(\rho_f E\right)^*$ and $\left(\rho_f \boldsymbol{u}\right)^*$ temporary variables are given by the following explicit expressions

$$\left(\rho_f E\right)^* = \left(\rho_f E\right)^n - \frac{\Delta t}{\varepsilon^3} \nabla \cdot \left(\boldsymbol{u} \rho_f \frac{u^2}{2}\right)^n \tag{11}$$

$$\left(\rho_f \boldsymbol{u}\right)^* = \left(\rho_f \boldsymbol{u}\right)^n - \varepsilon \Delta t \boldsymbol{F}_{\boldsymbol{d}}^n \tag{12}$$

Following a semi-implicit Euler method for Eq. (6) the semi-discrete thermal equation for the MCM takes the following form:

$$\begin{aligned} &\left(\frac{(1-\varepsilon)}{\Delta t} \rho_s c_H^n + (1-\varepsilon) \rho_s \left(\frac{\partial s_s}{\partial H}\right)_{T_s^n} \left(\frac{\partial H}{\partial t}\right)^{n+1} + h_c a_s\right) T_s^{n+1} \\ &- \nabla \cdot \left(k_s^{\mathrm{eff}} \nabla T_s^{n+1}\right) - h_c a_s \left(\frac{p^{n+1}}{R\rho_f^{n+1}}\right) = \frac{(1-\varepsilon)}{\Delta t} \rho_s c_H^n T_s^n \end{aligned} \tag{13}$$

Note that both Eqs. (10) and (13) are coupled through the convection source term. Consequently, the fluid pressure and solid temperature are simultaneously solved using a direct solver. Subsequently, the fluid temperature T_f is calculated using the equation of state (EOS). For the case of a packed bed solid matrix as presented in this work, the non-linear Darcy–Forchheimer relation Eq. (3) is treated semi-implicitly for the computation of the velocity at the new time-step $n+1$. Therefore $\mathbf{u}^{n+1}$ is computed as

$$\left(\rho_f^{n+1} + \varepsilon \Delta t \left(\frac{\mu}{K} + \frac{c_f \rho_f^n}{\sqrt{K}} |\mathbf{u}^n|\right)\right) \mathbf{u}^{n+1} = \left(\rho_f \mathbf{u}\right)^n - \varepsilon \Delta t \nabla p^{n+1} \tag{14}$$

3.2. Time integration of the LMN scheme

The integration in time of the LMN scheme bears similarities with the IMEX scheme. A uniform-Mach number method (Knikker, 2011) is adopted for its conservation properties in tandem with a pressure-correction method for computing the velocity field with the latter involving the numerical solution of a non-uniform coefficient Poisson equation for the pressure. First, the continuity equation is explicitly treated as shown in Eq. (7) for computing ρ_f^{n+1}. Second, the fluid temperature is computed from the EOS

$$T_f^{n+1} = \frac{p_0}{R\rho_f^{n+1}} \tag{15}$$

where p_0, as previously stated, is the constant reference pressure of the AMR. Note that in the IMEX scheme T_f^{n+1} is also computed by virtue of the EOS, albeit also including the spatially variable p_1 pressure contribution. The thermal equation for the solid matrix is integrated in time as shown in Eq. (13) with the only difference being on the explicit treatment of the convective term, namely

$$\begin{aligned} &\left(\frac{(1-\varepsilon)}{\Delta t} \rho_s c_H^n + (1-\varepsilon) \rho_s \left(\frac{\partial s_s}{\partial H}\right)_{T_s^n} \left(\frac{\partial H}{\partial t}\right)^{n+1}\right) T_s^{n+1} \\ &- \nabla \cdot \left(k_s^{\mathrm{eff}} \nabla T_s^{n+1}\right) = \frac{(1-\varepsilon)}{\Delta t} \rho_s c_H^n T_s^n - h_c a_s \left(T_f^n - T_s^n\right) \end{aligned} \tag{16}$$

The velocity at the new time step $\boldsymbol{u}^{n+1}$ is computed by first introducing an intermediate velocity $\boldsymbol{u}^*$, which is not to be confused with the temporary variable in Eq. (12). This intermediate velocity is computed by explicitly integrating the momentum equation Eq. (2) and treating the drag force Eq. (3) semi-implicitly

$$\left(\rho_f^{n+1} + \varepsilon \Delta t \left(\frac{\mu}{K} + \frac{c_f \rho_f^n}{\sqrt{K}} |\mathbf{u}^n|\right)\right) \mathbf{u}^* = \left(\rho_f \mathbf{u}\right)^n - \varepsilon \Delta t \nabla p^n \tag{17}$$

and is subsequently corrected to give the velocity $\boldsymbol{u}^{n+1}$

$$\boldsymbol{u}^{n+1} = \boldsymbol{u}^* - \frac{\varepsilon \Delta t}{\rho_f^{n+1}} \nabla p' \tag{18}$$

where p' is the pressure correction defined as $p' = p^{n+1} - p^n$. Taking the divergence of Eq. (18) leads to a variable coefficient pressure-Poisson equation with Dirichlet boundary conditions:

$$\nabla \cdot \left(\frac{1}{\rho_f^{n+1}} \nabla p'\right) = \frac{1}{\varepsilon \Delta t} \left(\nabla \cdot \boldsymbol{u}^* - \nabla \cdot \boldsymbol{u}^{n+1}\right) \tag{19}$$

During the flow stages, the Dirichlet boundary conditions are computed in a similar vein as for the IMEX scheme (see Section 3.4), using

the same root-finding technique and convergence criteria as given for evaluating the boundary conditions of p^{n+1}. The second term of the right-hand side of the pressure Poisson equation is derived by combining the EOS, Eq. (15), the continuity , Eq. (1), and the thermal energy equation for the fluid, Eq. (5), as

$$\nabla \cdot \boldsymbol{u}^{n+1} = \frac{\gamma - 1}{\gamma p_0} \left(\nabla \cdot \left(k_f^{\text{eff}} \nabla T_f^{n+1} \right) - h_c a_s \left(T_f^{n+1} - T_s^{n+1} \right) + \boldsymbol{F}_{\boldsymbol{d}}^{n} \cdot \boldsymbol{u}^{n} \right) \quad (20)$$

where $\boldsymbol{F}_{\boldsymbol{d}}^{n}$ is the drag force (see Eq. (3)) exerted on a fluid of density ρ_f^n with a velocity of $\boldsymbol{u}^n$.

3.3. Spatial discretization

The differential operators of the semidiscrete equations shown above are discretized in space using $O\left(\Delta x^2\right)$ centered finite differences both at the interior and boundary grid points. In Eq. (11), the enthalpy flux term $\nabla \cdot (h \nabla p)$ and the left-hand-side of Eq. (19) are discretized using second-order Lagrange interpolants as demonstrated in Boscheri and Pareschi (2021). Concerning the continuity, Eq. (7), the numerical flux term is discretized using a Rusanov-type Riemann solver also demonstrated in Ref. Boscheri and Pareschi (2021). Throughout this work, the spatial resolution for both models is kept the same for consistency across the test cases, following a respective convergence analysis. The chosen resolution of 480 spatial mesh points ensures that the relative convergence error is smaller than the tolerance required to achieve a cyclic steady state, as will be further discussed in Section 5.

3.4. Boundary conditions

Adiabatic boundaries are assumed for the solid matrix at the reservoirs throughout the AMR cycle; homogeneous Neumann boundary conditions are applied to Eq. (6) (Trevizoli and Barbosa, 2017). The boundary conditions for the fluid variables differ depending on the stage of the AMR cycle. For the velocity, only initial conditions are applied since the convective term of Eq. (2) is omitted.

During the two flow stages of the AMR cycle, only the temperatures of each reservoir and the targeted mass flow rate $\dot{m}_t$ are known. Nevertheless, pressure is implicitly coupled to the mass flow rate. Therefore, the pressure boundary, i.e., the pressure perturbation p_1, is unknown in the upstream reservoir, and consequently, the density of the fluid at the boundary needs to be specified so that the mass flow rate, $\dot{m}_n$, equals the target mass flow rate. Once the upstream pressure is known at the reservoir, a Dirichlet boundary condition is applied for the density by virtue of the equation of state, and a homogeneous Neumann boundary condition is applied to the opposite reservoir.

During the magnetization/demagnetization stages, the pressure at the reservoirs is equal to the reference pressure, and the boundary conditions for the density are homogeneous Neumann for both reservoirs. Note that throughout the cycle, the temperature of the fluid is computed using the equation of state. More details on the computation of the pressure boundary condition are presented in the following section.

3.4.1. Pressure boundary conditions during flow stages

The secant method is adopted to calculate the pressure boundary condition in the upstream reservoir, ensuring that the mass flow rate $\dot{m}_n$ at that reservoir is approximately equal, up to a certain tolerance, ϵ_m, to the target mass flow rate. Denoting k as the step within the root-finding loop, the new estimate of the pressure boundary value p_D^{k+1} is computed as:

$$p_D^{k+1} = p_D^k - \left(p_D^k - p_D^{k-1} \right) \frac{\dot{m}_n^k - \dot{m}_t}{\dot{m}_n^k - \dot{m}_n^{k-1}} \quad (21)$$

Note that the convergence of the secant method accelerates as the AMR cycle approaches its steady-state operation. A schematic of the IMEX scheme as well as the secant method iteration is shown in Fig. 2. The fluid/solid kernel of the IMEX model in Fig. 2 can be replaced with the respective kernel of the LMN model, i.e.,Eq.(15) to (19).

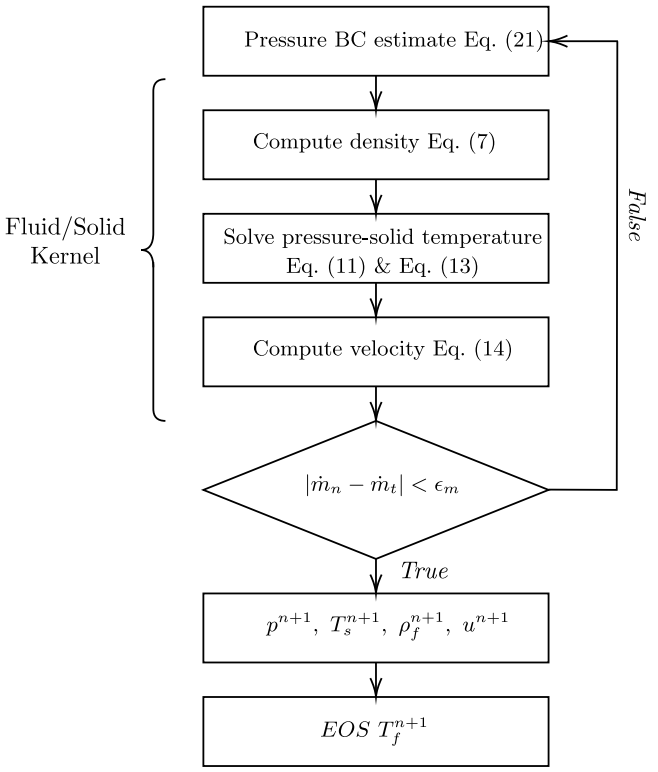

Fig. 2. Flow chart of the root-finding technique for the pressure boundary condition during the flow stages of the AMR. The flow chart includes the IMEX scheme for the discretization in time. The root-finding loop for a given time-step converges when the absolute difference between the targeted mass flow $\dot{m}_t$ and the numerically computed one, $\dot{m}_n$, is below a prescribed tolerance ϵ_m. Note that the temperature profile of the fluid T_f is computed using the equation of state (EOS).

4. Cycle convergence and performance metrics

The convergence criterion for the AMR cycle to have achieved periodicity, i.e., cyclic steady-state operation, is based on the work of Engelbrecht (2008). Specifically, denoting U_f as the internal energy of the fluid entrained within the regenerator under the assumptions of uniform porosity and cross-sectional area, A_c, it is given by the following expression

$$U_f(t) = \varepsilon A_c \int_0^L \rho_f c_v T_f \, dx \quad (22)$$

where L is the length of the regenerator, and $c_v = c_v(p, T_f)$ is the isochoric specific heat capacity of the working fluid. In a similar vein, the MCM's total energy is computed as

$$U_s(t) = (1 - \varepsilon) A_c \int_0^L c_H T_s \, dx. \quad (23)$$

where $c_H = c_H(s_s, T_s, H)$ The convergence criterion for the periodic operation of the AMR device is computed from the following expression

$$\frac{|U_f(\tau) - U_f(0)| - |U_s(\tau) - U_s(0)|}{\max(U_f + U_s) - \min(U_f + U_s)} < \epsilon_c \quad (24)$$

where τ is the period of the AMR cycle, ϵ_c is the prescribed tolerance, and $\max(U_f + U_s)$ and $\min(U_f + U_s)$ correspond to the maximum and minimum energy of the fluid and MCM, respectively, during the AMR cycle.

To quantify the performance of the AMR, the commonly used metrics also employed here are the cycle-average cooling, P_c, and heat

Table 1
Material properties for the two materials in the two-layer AMR and their uncertainties, obtained via a non-linear least-squares fit of the MFT model to the experimental data. T_{Curie} denotes the Curie temperature, g_j is the Landé factor, J represents the total angular momentum, θ_D stands for the Debye temperature, N_s refers to the number of spins per unit mass, M indicates the molar mass and γ_e is the Sommerfeld constant.

Material	$GdNi_2$	$Dy_{0.85}Er_{0.25}Al_2$
T_{Curie} [K]	77.78 ± 0.58	55.35 ± 1.04
g_j [-]	2.30 ± 0.18	3.49 ± 1.12
J [-]	2.69 ± 0.31	4.12 ± 1.83
θ_D [K]	304.7 ± 7.6	221.1 ± 19
N_s [10^{24} kg^{-1}]	2.44 ± 0.1	1.88 ± 0.2
M [kg/mol]	0.13 ± 0.008	0.46 ± 0.17
γ_e [J/kgK^2]	0.82 ± 0.09	1.6 ± 0.16

rejection power, P_h, which are defined as

$$P_c = \frac{1}{\tau}\int_0^\tau |\dot{m}_{hc}|\left(h(T_c, p_{ref}) - h(T_f, p)_{x=L}\right)\, dt$$
$$P_h = \frac{1}{\tau}\int_0^\tau |\dot{m}_{ch}|\left(h(T_f, p)_{x=0} - h(T_h, p_{ref})\right)\, dt \quad (25)$$

where $\dot{m}_{hc}$ is the mass flow rate after demagnetization, i.e., flow from the hot to the cold reservoir, $\dot{m}_{ch}$ is the mass flow rate in the opposite direction, and h is the specific enthalpy and p_{ref} is the pressure of the two reservoirs. T_c and T_h correspond to the constant temperatures of the cold and hot reservoirs, respectively. Note that in this study, the hot reservoir is located at $x = 0$, and the cold reservoir is at $x = L$. From Eq. (25), COP is defined as:

$$\text{COP} = \frac{P_c}{P_h - P_c} \quad (26)$$

5. Validation

This section validates the 1D AMR models presented in this study for compressible fluids. We consider the case of a AMR operating at cryogenic temperatures and employing helium gas as the working fluid. The validation benchmark is derived from the experimental work conducted by Park and Jeong (2017), which has also previously been used to validate numerical AMR models (Zheng et al., 2023). Following the methodology of Zheng et al. (2023), only the first stage of the AMR device is modeled. The material properties of the magnetocaloric materials used by Park and Jeong (2017), specifically $GdNi_2$ and $Dy_{0.85}Er_{0.25}Al_2$ alloys, are known from literature (Gschneidner et al., 1997; Zimm et al., 1991). However, to ensure material data is available at all fields and temperatures and to have a fully consistent material data set, the Mean-Field-Theory (MFT) model was fitted to the experimental material properties by performing a non-linear least squares fit. The MFT is extensively used to model second order materials for a range of AMR temperatures (Bjørk and Engelbrecht, 2011; Matsumoto et al., 2011; Aprea et al., 2012). More details regarding the underlying theory of the model can be found in Smith et al. (2012). Subsequently, after the validation study, the computed MFT-parameters are utilized to generate the magnetocaloric properties of these alloys under different applied magnetic fields compared to those used in the original experimental data. We assume that the internal magnetic field is equal to the applied magnetic field, i.e., demagnetization effects are ignored. Fig. 3 shows an example of the fitted properties for $Dy_{0.85}Er_{0.25}Al_2$. The Mean-Field-Theory (MFT) parameters for both alloys are detailed in Table 1 and the resulting properties for the applied magnetic fields of interest are shown in Fig. 3.

The parameters used for modeling the AMR device are as follows: the device's length is set at $L = 120$ mm with a cylindrical packed bed having a diameter of $D = 21.6$ mm. The first layer of the packed bed is filled with $GdNi_2$ up to a height of 48 mm, and the remaining packed bed contains $Dy_{0.85}Er_{0.25}Al_2$. The spherical particles are assumed to have a uniform diameter of $d_p = 500\,\mu$m and a uniform porosity of $\varepsilon = 0.5$.

The first layer of MCM is taken to have the density of Gd, $\rho_s = 7901$ kg/m^3 (Wilthan et al., 2017), and a thermal conductivity of $k_s = 5$ W/m K (Watanabe et al., 2021). For the second layer, the thermophysical properties of Dy are used, i.e. density $\rho_s = 8551$ kg/m^3 (Wilthan et al., 2017) and thermal conductivity $k_s = 11$ W/m K (Ho et al., 1972). Here we take the reference pressure to be $p_{ref} = 5$ bar, which, while falling within the reported pressure range for the He reservoirs (Park and Jeong, 2017), might vary depending on the magnitude of the mass flow rate. We note that the density of the working fluid, ρ_f, is not constant throughout the AMR, as will also be discussed subsequently.

The magnetization and mass flow rate profiles used in Park and Jeong (2017), Zheng et al. (2023) for a period of the AMR cycle, $\tau = 20$ s, are shown in Fig. 4. The applied magnetic field is assumed to be uniform across the regenerator, reaching a maximum value of 3 T. As can be seen from the figure, the mass flow rate is discontinuous at the start/end of each blow period. Therefore, during the beginning of the two flow stages the mass flow rate is gradually increased via the use of Hermite interpolants to avoid any jump discontinuities of the velocity field. The maximum amplitude of the mass flow rate is determined based on the total mass, i.e. the shuttle mass, of the working fluid flowing through the regenerator during each flow stage of the AMR cycle. Specifically, it is set to either 1.1 g or 2.8 g as per the experimental results (Park and Jeong, 2017). Additionally, the total number of equispaced grid points remains constant at $N_x = 480$. The time-step value is set equal to 7.27×10^{-4} s and 2.85×10^{-4} s for the 1.1 g and 2.8 g shuttle masses respectively. The tolerance for the cyclical steady-state operation of the AMR is set at $\epsilon_c = 10^{-3}$, and the tolerance for the targeted mass flow rate is set at $\epsilon_m = 10^{-8}$ (cf. Fig. 2).

5.1. Comparison of the 1D models with experimental and 2D numerical data

Fig. 5 shows the cooling power, P_c, of the AMR setup discussed in the previous section, plotted against the temperature of the cold reservoir T_c, while maintaining the temperature of the hot reservoir T_h at a constant 77 K. Two shuttle mass values are considered. Also shown are the P_c values obtained from the numerical results of Zheng et al. (2023) and the experimental data of Park and Jeong (2017).

The models presented in this work demonstrate close agreement with both previous numerical and experimental results. Differences in the computed P_c among the two 1D models are attributed to the implicit or explicit treatment of the coupling heat convection term and the variations in time integration schemes, such as the projection of the velocity field. In general, the results from both 1D models are consistent with each other and display a similar trend. Regarding the comparison between the 2D numerical and experimental data, specifically for a shuttle mass of 2.8 g, the 1D models closely align with the numerical results of Zheng et al. (2023). The larger deviations observed in the 1D models for the smaller shuttle mass 1.1 g compared to both numerical and experimental results warrant further investigation. Uncertainties in the operational pressure and potentially ambiguous boundary conditions used in the AMR cycles of Zheng et al. (2023) could be contributing factors. With regards to the discrepancy to experimental results these can be attributed to assumptions made when employing the 1D AMR model. These assumptions include the absence of heat losses, uniform porosities and particle size, demagnetization, material properties generated by the MFT, and differences in the structure of the mass flow rate profiles compared to the experimental profiles of Park and Jeong (2017). Despite these assumptions in the 1D models presented here, their efficacy in capturing the performance of an AMR device at cryogenic temperatures using a compressible working fluid is validated.

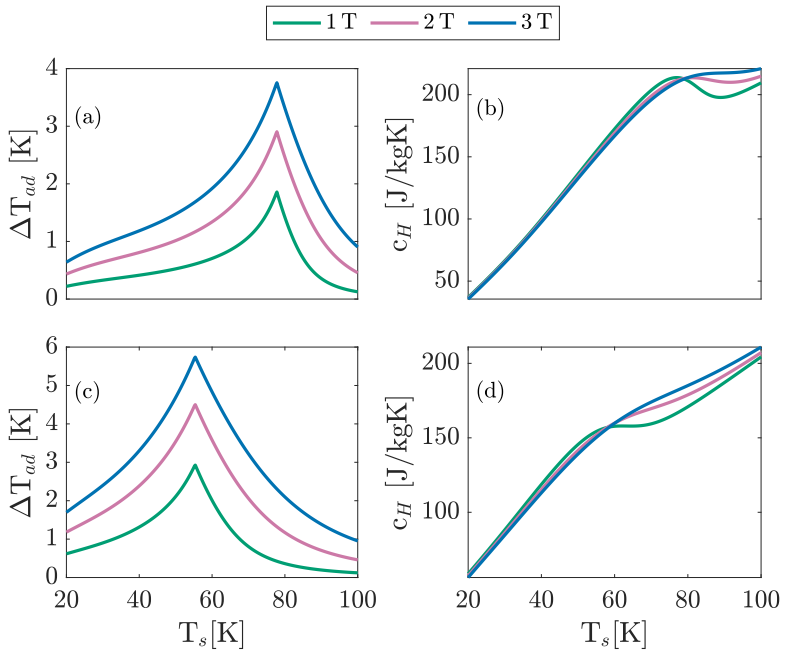

Fig. 3. Adiabatic temperature and specific heat capacity for different applied magnetic fields for the first (a-b), $GdNi_2$, and second (c-d), $Dy_{0.85}Er_{0.25}Al_2$, layer of the AMR device in Park and Jeong (2017). The values are generated via the MFT model for the parameters given in Table 1.

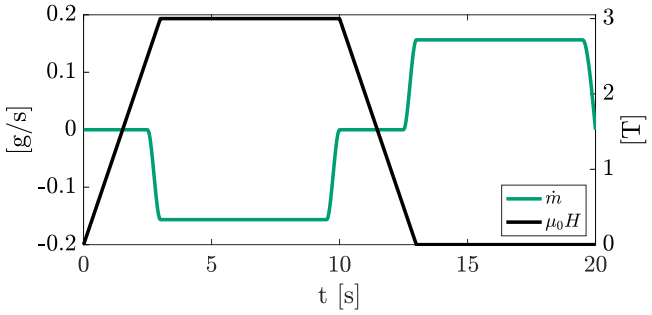

Fig. 4. Applied magnetic field (black) and mass flow rate profile (green) within an AMR cycle for the benchmark test-case of Park and Jeong (2017). The amplitude of the mass flow rate shown in this figure is computed for the mass of He to be flowing through during each fluid stage to be equal to 1.1 g. (For interpretation of the references to color in this figure legend, the reader is referred to the web version of this article.)

6. A cryogenic test-case: Comparing the compressible and incompressible models

It is important to explore the differences between the compressible 1D AMR models presented in this work and the previous incompressible 1D AMR model upon which this new model is based (Lei et al., 2015, 2016). This investigation will highlight the use cases for which the incompressible model cannot be correctly applied. Here, we assess the impact of the incompressibility constraint at cryogenic temperatures on the estimation of the cooling power within the designed AMR cycle, a critical factor influencing the production of liquid hydrogen.

We consider a test case for hydrogen liquefaction where the magnetic cooling device consists of a single-layer packed bed of spherical particles, detailed subsequently, and the magnetic field is generated by a superconducting magnet. For the latter, we assume a 19 T magnitude applied field, which follows a Gaussian profile with the peak at 100 cm and a standard deviation of $\sqrt{19}$. This field profile is chosen to allow for easy reproduction of this work, and the profile is shown in Fig. 6. The regenerator's motion, occurring from left to right during magnetization and in the opposite direction during demagnetization, results in the cold side experiencing the maximum applied field instantaneously twice within each cycle. This occurs as it passes the center maximum field value twice, as illustrated in Fig. 6. Thus, the applied field is not homogeneous across the AMR. The mass flow rate profile has the same structure as the one shown in Fig. 4 for all the examined mass flow rate amplitudes.

Although many MCMs have demonstrated a large magnetocaloric effect at cryogenic temperatures (Bykov et al., 2024), the purpose of this study is to showcase the impact of assumptions made in the fluid part of the AMR model, which are independent of the choice of MCM. For this purpose, a single layer of $Dy_{0.85}Er_{0.25}Al_2$ is used, with fixed hot and cold reservoir temperatures set at $T_h = 61$ K and $T_c = 51$ K, respectively. Magnetic properties are derived using the parameters fitted through the MFT model, as presented in Table 1. The thermophysical properties are consistent with those previously reported in Section 5.

The cylindrical packed-bed is assumed to have dimensions $L = 25$ cm in length and $D = 15$ cm in diameter. Both the porosity ϵ and the diameter of the spherical particles d_p correspond to those used in Section 5. The operating pressure of the AMR cycle is set to 15 bar. The operating frequency is 0.05 Hz, and the individual AMR flow periods and magnetization/demagnetization steps are 7 and 3 s, respectively. All simulations were conducted with a resolution of $N_x = 480$ grid points and a time step Δt calculated as

$$\Delta t = \mathrm{CFL}\frac{\Delta x}{u_h/\epsilon} = \mathrm{CFL}\frac{\Delta x \epsilon A_c \rho_h}{\max(\dot{m})} \tag{27}$$

where CFL = 0.8 denotes the Courant–Friedrichs–Lewy number (Kundu et al., 2015) for both the IMEX and LMN solver. Additionally, u_h is the maximum superficial velocity entering the AMR during the hot-to-cold stage of the cycle, where ρ_h denotes the density of the fluid at the reference pressure and temperature of the hot reservoir.

For the incompressible solver, the thermophysical properties of helium are set to be constant and equal to the average temperature of the two reservoirs at the reference pressure. Furthermore, the density of helium is also set to be constant and computed again from the reference pressure and the average temperature of the two reservoirs through the EOS. The computed cooling power for the described temperature span for both the compressible and incompressible models is shown

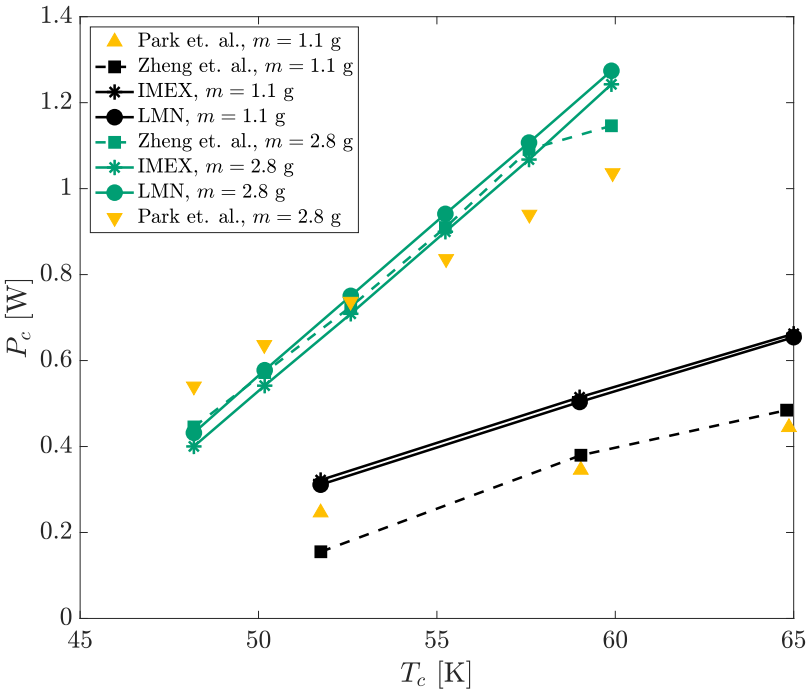

Fig. 5. Cooling power of the AMR setup of Park and Jeong (2017) as a function of temperature of the cold reservoir T_c. The temperature of the hot reservoir is kept constant to $T_h = 77$ K. Results are shown for two values of shuttle mass and compared to the experimental data of Park and Jeong (2017) and the numerical results of Zheng et al. (2023).

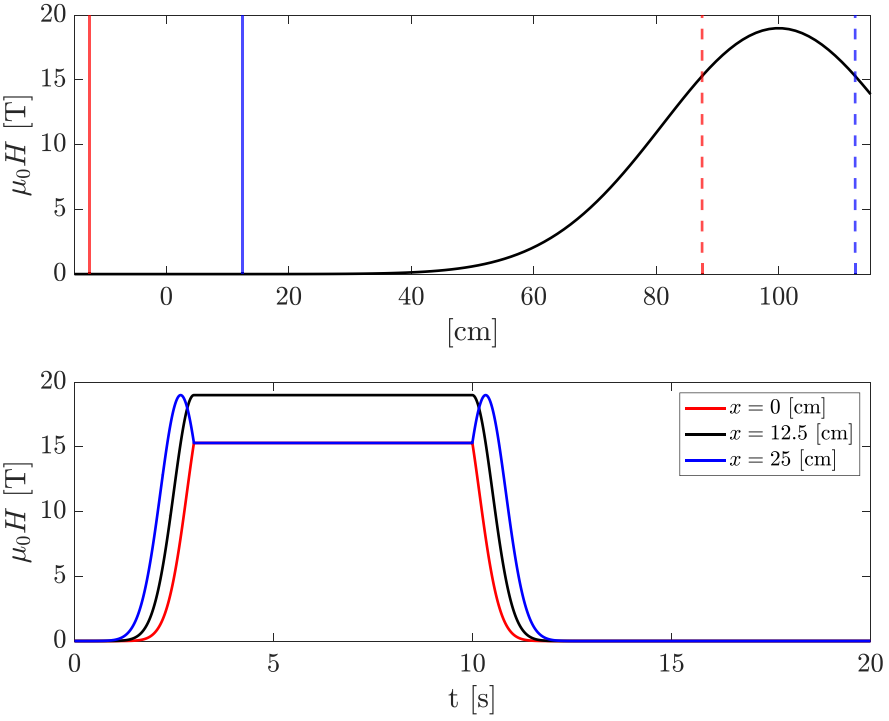

Fig. 6. Top: Spatial structure of the applied magnetic field (black) with a maximum amplitude of 19 T. The vertical lines indicate the locations of the hot (red) and cold (blue) reservoirs relative to the applied magnetic field. The dashed lines correspond to the location of the regenerator when the maximum magnetic field is applied while the solid lines correspond to the location of the regenerator during the demagnetization stage of the cycle. Bottom: Applied magnetic field profiles at the magnetization step at different axial locations of the regenerator, derived from the profile shown at the top of this figure. The cycle time is $\tau = 20$ s. (For interpretation of the references to color in this figure legend, the reader is referred to the web version of this article.)

in Fig. 7. As observed from the figure, at low mass flow rates, both compressible and incompressible solvers yield nearly identical cooling powers. However, as the mass flow rate increases, the compressible models reach their peak cooling power at significantly lower flow rates than the incompressible model. As depicted in Fig. 8, for larger mass flow rates, during the two flow stages of the AMR, the density of helium within the porous bed is close and even equal to either the hot reservoir (for the hot-to-cold flow stage of the AMR cycle) or the cold reservoir (for the opposite flow direction). Therefore, the thermal mass that each reservoir encounters deviates greatly from the average

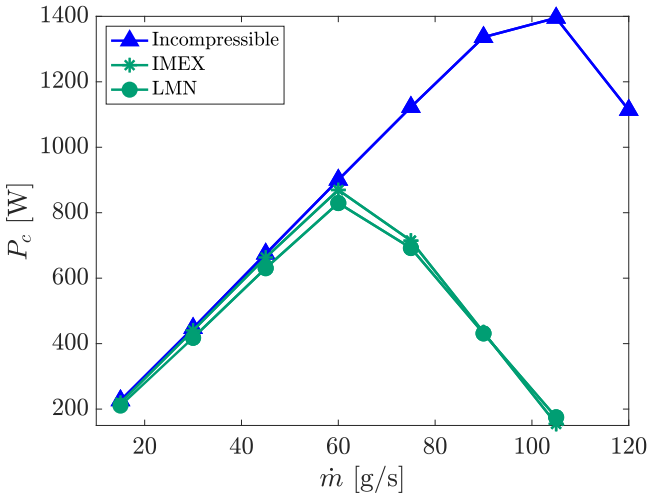

Fig. 7. Cooling power as a function of mass flow rate for the compressible 1D solvers presented in this work and the incompressible 1D solver in Refs. Engelbrecht (2008), Lei et al. (2015, 2016, 2017).

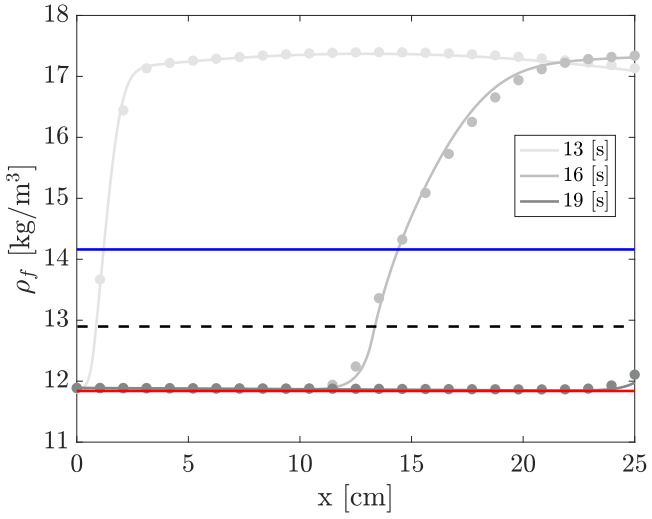

Fig. 8. Comparison of density profiles between the compressible and incompressible solvers for a maximum mass flow rate of 75 g/s. Solid blue and red lines are the helium density of the cold and hot reservoirs, respectively, computed at a reference pressure of 15 bar. The dashed black line corresponds to the density value used for the incompressible solver. Density profiles (solid lines) of the compressible IMEX solver, and a subset of the density values of the LMN solver (solid circles), are shown at three distinct time instances during the hot-to-cold flow stage of the AMR cycle (cf. Fig. 4), for which the cooling power is computed (see Eq. (25)). (For interpretation of the references to color in this figure legend, the reader is referred to the web version of this article.)

density value used in the incompressible solver. This results in the incompressible approximation overestimating not only the maximum value of the cooling power of the AMR device but also the optimum operating mass flow rate for this given configuration. Thus, it highlights the importance of using a compressible model for compressible heat transfer fluids at cryogenic temperatures.

7. Conclusions

Modeling of an AMR operating at cryogenic temperatures for hydrogen liquefaction necessitates the use of a compressible working fluid. The large temperature span drives a substantial density difference of the working fluid across the regenerator, which can significantly affect the predicted metrics if this density variation is not adequately accounted for. Two 1D models of an AMR, both developed in MATLAB (The MathWorks Inc, 2023), which take into account the compressibility of the working fluid were presented. The fully coupled time-dependent system of equations for the fluid is solved using discretizations which consider the inherent stiffness of such low Mach number flows encountered in a porous medium like the magnetic regenerator.

Two different approaches are followed for the time integration of the model equations. One approach involves an all-Mach numbers IMEX scheme, which treats the continuity and momentum equations explicitly. In this scheme, an elliptic pressure-wave equation, derived through the total energy equation of the fluid, is solved implicitly, coupled to the thermal energy equation of the solid matrix via the convection term. The second approach is based on the asymptotic expansion of the compressible Navier–Stokes equations for low-Mach number flows, i.e., LMN scheme. In this approach, the continuity equation is treated explicitly, while the temperature of the fluid is computed using the equation of state and the reference, i.e., thermodynamic pressure of the fluid. The temperature of the solid is computed by treating the convective coupling term explicitly. The velocity field is subsequently evaluated by following a pressure-correction scheme. An intermediate velocity is corrected by the computed pressure-correction term, with the latter being computed by numerically solving a variable-coefficient Poisson equation.

Regarding the capabilities of the two models, the IMEX-based model is preferable for more generalized configurations within a porous medium context due to its all-Mach number stiffly-stable scheme. This makes it suitable for applications with smaller porosities, which induce higher fluid-flow velocities, as well as different solid-matrix geometries such as parallel plates. In contrast, the LMN model offers easier development due to its foundation on an incompressible time-splitting scheme. This facilitates the individual validation of its components and its integration into existing CFD solvers. However, the Mach limit for the LMN model requires further investigation in the context of porous media and should be compared to the IMEX model specifically for highly porous media applications. Additionally, the reference pressure for large porosities within the AMR may affect the overall accuracy of the method due to the substantial pressure drop within the solid matrix. This issue, which also needs to be addressed in future work, can potentially be corrected by including the computation of the reference pressure per time-step, as demonstrated by Knikker (2011).

The correlations used and the drag force of the porous medium exerted to the fluid can be adapted to allow the investigation of different regenerator geometries. During the flow stages of the AMR cycle, the targeted mass flow rate is implicitly enforced through the Dirichlet boundary condition when solving the elliptic equation for the pressure in both models. A simple non-linear root-finding technique is employed, computing the value of the pressure at the upstream boundary in such a way that the numerically computed mass flow rate equals the targeted one up to a prescribed tolerance.

The compressible AMR cycle models are validated by comparing the computed cooling power against numerical and experimental results. The material properties data were generated using a mean-field-theory model, and overall, the two models exhibit good agreement when compared to the experimental data. A one-layer test case at cryogenic temperatures is also presented. The applied magnetic field varied both in space and in time, following a Gaussian profile. The purpose of this benchmark was to showcase a test case that can be easily replicated and thus used as a future validation benchmark among different AMR models at cryogenic temperatures. Furthermore, a comparison of the computed cooling power as a function of the targeted mass flow rate between the developed models and an incompressible AMR model is provided. This study demonstrates that the incompressible model significantly overestimates the predicted cooling power and optimal mass flow rate range under the assumption of a constant-density fluid. This finding highlights the necessity for solvers used to model an AMR

at cryogenic temperatures to account for the large density variations of the working fluid. In this context, the effects of both geometric and operational parameters need to be reconsidered and evaluated for their impact on the predicted performance of a cryogenic AMR. Additionally, the influence of alternative geometries beyond packed beds should be investigated.

CRediT authorship contribution statement

Theodoros Diamantopoulos: Conceptualization, Data curation, Investigation, Methodology, Software, Validation, Visualization, Writing – original draft, Writing – review & editing. **Tommaso Matteuzzi:** Data curation, Validation, Visualization. **Rasmus Bjørk:** Conceptualization, Funding acquisition, Investigation, Project administration, Resources, Supervision, Writing – original draft, Writing – review & editing.

Declaration of competing interest

The authors declare that they have no known competing financial interests or personal relationships that could have appeared to influence the work reported in this paper.

Acknowledgments

We acknowledge funding from the EU-funded project HyLICAL. This project has received funding from the Europeans Union's Horizon Europe research and innovation program under grant agreement No 101101461. The project is supported by the Clean Hydrogen Partnership and its members. We also acknowledge funding from the Norwegian Research Council project 336403 entitled "Hydrogen Liquefaction with Caloric materials" (LIQUID-H).

References

Adapa, Sarath R, Feng, Tianshi, Ihnfeldt, Robin V, Chen, Renkun, 2024. Optimisation of a packed particle magnetocaloric refrigerator: A combined experimental and theoretical study. Int. J. Refrig. 159, 64–73.

Ansarinasab, Hojat, Fatimah, Manal, Khojasteh-Salkuyeh, Yaser, 2023. Conceptual design of two novel hydrogen liquefaction processes using a multistage active magnetic refrigeration system. Appl. Therm. Eng. 230, 120771.

Aprea, Ciro, Greco, Adriana, Maiorino, Angelo, 2012. Modelling an active magnetic refrigeration system: A comparison with different models of incompressible flow through a packed bed. Appl. Therm. Eng. 36, 296–306.

Archipley, Corey, Barclay, John, Meinhardt, Kerry, Whyatt, Greg, Thomsen, Edwin, Holladay, Jamie, Cui, Jun, Anderson, Iver, Wolf, Sam, 2022. Methane liquefaction with an active magnetic regenerative refrigerator. Cryogenics 128, 103588.

Barclay, John, Brooks, Kriston, Cui, Jun, Holladay, Jamelyn, Meinhardt, Kerry, Polikarpov, Evgueni, Thomsen, Edwin, 2019. Propane liquefaction with an active magnetic regenerative liquefier. Cryogenics 100, 69–76.

Barletta, Antonio, 2015. On the thermal instability induced by viscous dissipation. Int. J. Therm. Sci. 88, 238–247.

Bejan, Adrian, 2013. Convection Heat Transfer. John Wiley & Sons.

Bell, Ian H., Wronski, Jorrit, Quoilin, Sylvain, Lemort, Vincent, 2014. Pure and Pseudo-pure Fluid Thermophysical Property Evaluation and the Open-Source Thermophysical Property Library CoolProp. Ind. Eng. Chem. Res. 53 (6), 2498–2508. http://dx.doi.org/10.1021/ie4033999, URL http://pubs.acs.org/doi/abs/10.1021/ie4033999.

Bird, R. Byron, Stewart, Warren E., Lightfoot, Edwin N., 2002. Transport Phenomena, vol. 1, John Wiley & Sons.

Bjørk, Rasmus, Engelbrecht, Kurt, 2011. The influence of the magnetic field on the performance of an active magnetic regenerator (AMR). Int. J. Refrig. 34 (1), 192–203.

Boscheri, Walter, Pareschi, Lorenzo, 2021. High order pressure-based semi-implicit IMEX schemes for the 3D Navier-Stokes equations at all Mach numbers. J. Comput. Phys. 434, 110206.

Burdyny, Thomas, Rowe, Andrew, 2013. Simplified modeling of active magnetic regenerators. Int. J. Refrig. 36 (3), 932–940.

Bykov, E, Karpenkov, A, Liu, W, Straßheim, M, Niehoff, T, Skokov, K, Scheibel, F, Gutfleisch, O, Mejía, C Salazar, Wosnitza, J, et al., 2024. Magnetocaloric effect in the laves phases RCo2 (R=Er, Ho, Dy, and Tb) in high magnetic fields. J. Alloys Compd. 977, 173289.

Capovilla, Matheus S, Lozano, Jaime A, Trevizoli, Paulo V, Barbosa, Jr., Jader R, 2016. Performance evaluation of a magnetic refrigeration system. Sci. Technol. Built Environ. 22 (5), 534–543.

Costa, VAF, 2006. On natural convection in enclosures filled with fluid-saturated porous media including viscous dissipation. Int. J. Heat Mass Transfer 49 (13–14), 2215–2226.

DeGroot, Christopher T., Straatman, Anthony G., 2011. Closure of non-equilibrium volume-averaged energy equations in high-conductivity porous media. Int. J. Heat Mass Transfer 54 (23–24), 5039–5048.

Engelbrecht, Kurt, 2008. A Numerical Model of an Active Magnetic Regenerator with Experimental Validation (Ph. D. Thesis). University of Wisconsin-Madison.

Eriksen, Dan, Engelbrecht, Kurt, Bahl, CRH, Bjørk, Rasmus, Nielsen, Kaspar Kirstein, Insinga, Andrea Roberto, Pryds, Nini, 2015. Design and experimental tests of a rotary active magnetic regenerator prototype. Int. J. Refrig. 58, 14–21.

Eriksen, Dan, Engelbrecht, Kurt, Haffenden Bahl, Christian Robert, Bjørk, Rasmus, 2016. Exploring the efficiency potential for an active magnetic regenerator. Sci. Technol. Built Environ. 22 (5), 527–533.

Feng, Tianshi, Chen, Renkun, Ihnfeldt, Robin V., 2020. Modeling of hydrogen liquefaction using magnetocaloric cycles with permanent magnets. Int. J. Refrig. 119, 238–246.

Ghorbani, Bahram, Zendehboudi, Sohrab, Saady, Noori M Cata, Duan, Xili, Albayati, Talib M, 2023. Strategies to improve the performance of hydrogen storage systems by liquefaction methods: a comprehensive review. ACS Omega 8 (21), 18358–18399.

Gómez, J Romero, Garcia, R Ferreiro, Catoira, A De Miguel, Gómez, M Romero, 2013. Magnetocaloric effect: A review of the thermodynamic cycles in magnetic refrigeration. Renew. Sustain. Energy Rev. 17, 74–82.

Gottschall, Tino, Gracia-Condal, Adria, Fries, Maximilian, Taubel, Andreas, Pfeuffer, Lukas, Manosa, Lluis, Planes, Antoni, Skokov, Konstantin P, Gutfleisch, Oliver, 2018. A multicaloric cooling cycle that exploits thermal hysteresis. Nat. Mater. 17 (10), 929–934.

Gschneidner, K.A., Pecharsky, V.K., Malik, S.K., 1997. The (Dy 1-x Er x) Al 2 alloys as active magnetic regenerators for magnetic refrigeration. Adv. Cryog. Eng. Mater. 475–483.

Hadley, G.R., 1986. Thermal conductivity of packed metal powders. Int. J. Heat Mass Transfer 29 (6), 909–920.

Ho, Cho Yen, Powell, Ralph Waterbury, Liley, Peter E., 1972. Thermal conductivity of the elements. J. Phys. Chem. Ref. Data 1 (2), 279–421.

Jarauta, Alex, Zingan, Valentin, Minev, Peter, Secanell, Marc, 2020. A compressible fluid flow model coupling channel and porous media flows and its application to fuel cell materials. Transp. Porous Media 134 (2), 351–386.

Kamiya, Koji, Matsumoto, Koichi, Numazawa, Takenori, Masuyama, Shinji, Takeya, Hiroyuki, Saito, Akiko T., Kumazawa, Naoya, Futatsuka, Kazumi, Matsunaga, Keigo, Shirai, Tsuyoshi, Takada, Suguru, Iida, Teruhito, 2022. Active magnetic regenerative refrigeration using superconducting solenoid for hydrogen liquefaction. Appl. Phys. Express 15 (5), 053001.

Kaviany, Maasoud, 2012. Principles of Heat Transfer in Porous Media. Springer Science & Business Media.

Kim, John, Moin, Parviz, 1985. Application of a fractional-step method to incompressible Navier-Stokes equations. J. Comput. Phys. 59 (2), 308–323.

Kitanovski, Andrej, 2020. Energy applications of magnetocaloric materials. Adv. Energy Mater. 10 (10), 1903741.

Kitanovski, Andrej, Tušek, Jaka, Tomc, Urban, Plaznik, Uroš, Ožbolt, Marko, Poredoš, Alojz, 2016. Magnetocaloric Energy Conversion. Springer.

Knikker, Ronnie, 2011. A comparative study of high-order variable-property segregated algorithms for unsteady low Mach number flows. Int. J. Numer. Methods Fluids 66 (4), 403–427.

Kundu, Pijush K., Cohen, Ira M., Dowling, David R., 2015. Fluid Mechanics. Academic Press.

Lei, Tian, Engelbrecht, Kurt, Nielsen, Kaspar Kirstein, Bez, H Neves, Bahl, CRH, 2016. Study of multi-layer active magnetic regenerators using magnetocaloric materials with first and second order phase transition. J. Phys. D: Appl. Phys. 49 (34), 345001.

Lei, Tian, Engelbrecht, Kurt, Nielsen, Kaspar K, Veje, Christian T, 2017. Study of geometries of active magnetic regenerators for room temperature magnetocaloric refrigeration. Appl. Therm. Eng. 111, 1232–1243.

Lei, Tian, Nielsen, Kaspar K, Engelbrecht, Kurt, Bahl, Christian RH, Neves Bez, Henrique, Veje, Christian T, 2015. Sensitivity study of multi-layer active magnetic regenerators using first order magnetocaloric material La (Fe, Mn, Si) 13Hy. J. Appl. Phys. 118 (1).

Li, Zhiyong, Zhang, Huaibao, Liu, Yu, McDonough, James M., 2020. Implementation of compressible porous–fluid coupling method in an aerodynamics and aeroacoustics code part I: Laminar flow. Appl. Math. Comput. 364, 124682.

Liu, Wei, Gottschall, Tino, Scheibel, Franziska, Bykov, Eduard, Aubert, Alex, Fortunato, Nuno, Beckmann, Benedikt, Döring, Allan M, Zhang, Hongbin, Skokov, Konstantin, et al., 2024. A matter of performance and criticality: a review of rare-earth-based magnetocaloric intermetallic compounds for hydrogen liquefaction. J. Alloys Compd. 174612.

Liu, Qianlong, Vasilyev, Oleg V., 2007. A Brinkman penalization method for compressible flows in complex geometries. J. Comput. Phys. 227 (2), 946–966.

Macdonald, I.F., El-Sayed, M.S., Mow, K., Dullien, FAL, 1979. Flow through porous media-the Ergun equation revisited. Ind. Eng. Chem. Fundam. 18 (3), 199–208.

Matsumoto, Koichi, Kondo, Takuya, Ikeda, Masakazu, Numazawa, Takenori, 2011. Numerical analysis of active magnetic regenerators for hydrogen magnetic refrigeration between 20 and 77 K. Cryogenics 51 (6), 353–357.

Mößner, Michael, Radespiel, Rolf, 2015. Modelling of turbulent flow over porous media using a volume averaging approach and a Reynolds stress model. Comput. & Fluids 108, 25–42.

Müller, Bernhard, 1998. Low-Mach-number asymptotics of the Navier-Stokes equations. In: Floating, Flowing, Flying: Pieter J. Zandbergen's Life as Innovator, Inspirator and Instigator in Numerical Fluid Dynamics. Springer, pp. 97–109.

Nakashima, A.T.D., Peixer, G.F., Lozano, J.A., Barbosa, Jr., J.R., 2022. A lumped-element magnetic refrigerator model. Appl. Therm. Eng. 204, 117918.

Nield, D.A., 2007. The modeling of viscous dissipation in a saturated porous medium. J. Heat Transfer 129 (10), 1459–1463.

Nield, Donald A., Bejan, Adrian, et al., 2006. Convection in Porous Media, vol. 3, Springer.

Numazawa, T., Kamiya, K., Utaki, T., Matsumoto, K., 2014. Magnetic refrigerator for hydrogen liquefaction. Cryogenics 62, 185–192.

Paolucci, Samuel, 1982. Filtering of Sound from the Navier-Stokes Equations. Technical Report, Sandia National Laboratories.

Park, Inmyong, Jeong, Sangkwon, 2017. Development of the active magnetic regenerative refrigerator operating between 77 K and 20 K with the conduction cooled high temperature superconducting magnet. Cryogenics 88, 106–115.

Park, Inmyong, Kim, Youngkwon, Park, Jiho, Jeong, Sangkwon, 2015. Design method of the layered active magnetic regenerator (AMR) for hydrogen liquefaction by numerical simulation. Cryogenics 70, 57–64.

Restelli, Federica, Spatolisano, Elvira, Pellegrini, Laura A, Cattaneo, Simone, De Angelis, Alberto R, Lainati, Andrea, Roccaro, Ernesto, 2024. Liquefied hydrogen value chain: A detailed techno-economic evaluation for its application in the industrial and mobility sectors. Int. J. Hydrog. Energy 52, 454–466.

Rochette, David, Clain, Stéphane, 2005. Local heat transfer of compressible fluid in porous media: application to the HBC fuse. Int. J. Heat Fluid Flow 26 (2), 322–333.

Rowe, Andrew, 2012. Thermodynamics of active magnetic regenerators: Part I. Cryogenics 52 (2–3), 111–118.

Silva, Daniel J., Ventura, Joao, Araujo, Joao P., 2021. Caloric devices: A review on numerical modeling and optimization strategies. Int. J. Energy Res. 45 (13), 18498–18539.

Smaïli, Arezki, Aït-Ali, Samir, Chahine, Richard, 2011. Performance predictions of a first stage magnetic hydrogen liquefier. Int. J. Hydrog. Energy 36 (6), 4169–4177.

Smith, Anders, Bahl, Christian RH, Bjørk, Rasmus, Engelbrecht, Kurt, Nielsen, Kaspar K, Pryds, Nini, 2012. Materials challenges for high performance magnetocaloric refrigeration devices. Adv. Energy Mater. 2 (11), 1288–1318.

Tang, Xin, Sepehri-Amin, H, Terada, N, Martin-Cid, A, Kurniawan, I, Kobayashi, S, Kotani, Y, Takeya, H, Lai, J, Matsushita, Y, et al., 2022. Magnetic refrigeration material operating at a full temperature range required for hydrogen liquefaction. Nature Commun. 13 (1), 1817.

Taskaev, Sergey, Khovaylo, Vladimir, Skokov, Konstantin, Liu, Wei, Bykov, Eduard, Ulyanov, Maxim, Bataev, Dmitriy, Basharova, Anastasiya, Kononova, Marina, Plakhotskiy, Daniil, et al., 2020. Magnetocaloric effect in GdNi2 for cryogenic gas liquefaction studied in magnetic fields up to 50 T. J. Appl. Phys. 127 (23).

Teng, Ho, Zhao, T.S., 2000. An extension of Darcy's law to non-Stokes flow in porous media. Chem. Eng. Sci. 55 (14), 2727–2735.

Teyber, Reed, Holladay, Jamelyn, Meinhardt, Kerry, Polikarpov, Evgueni, Thomsen, Edwin, Cui, Jun, Rowe, Andrew, Barclay, John, 2019. Performance investigation of a high-field active magnetic regenerator. Appl. Energy 236, 426–436.

The MathWorks Inc, 2023. MATLAB version: 9.14.0 (R2023a). URL https://www.mathworks.com.

Trevizoli, Paulo V., Barbosa, Jr., Jader R., 2017. Thermal-hydraulic behavior and influence of carryover losses in oscillating-flow regenerators. Int. J. Therm. Sci. 113, 89–99.

Waske, Anja, Gruner, Markus E, Gottschall, Tino, Gutfleisch, Oliver, 2018. Magnetocaloric materials for refrigeration near room temperature. MRS Bull. 43 (4), 269–273.

Watanabe, S, Komatsu, S, Futatsuka, K, Kumazawa, N, Matsumoto, K, Kamiya, K, Takeya, H, Numazawa, T, 2021. Thermal expansion and thermal conductivity of RT 2 (R: Gd, Dy, Er; T: Al, Ni) intermetallic compounds for magnetic refrigerator. In: Journal of Physics: Conference Series. IOP Publishing.

Wilthan, Boris, Pfeif, Erik A, Diky, Vladimir V, Chirico, Robert D, Kattner, Ursula R, Kroenlein, Kenneth, 2017. Data resources for thermophysical properties of metals and alloys, part 1: structured data capture from the archival literature. CALPHAD 56, 126–138.

Zhang, Tongtong, Uratani, Joao, Huang, Yixuan, Xu, Lejin, Griffiths, Steve, Ding, Yulong, 2023a. Hydrogen liquefaction and storage: Recent progress and perspectives. Renew. Sustain. Energy Rev. 176, 113204.

Zhang, Yikun, Ying, Jiayu, Gao, Xinqiang, Mo, Zhaojun, Shen, Jun, Li, Lingwei, 2023b. Exploration of the rare-earth cobalt nickel-based magnetocaloric materials for hydrogen liquefaction. J. Mater. Sci. Technol. 159, 163–169.

Zheng, Wenshuai, Shen, Jun, Li, Zhenxing, Huang, Hongmei, Hai, Peng, Liu, Jun, Chen, Zhuo, Gao, Xinqiang, Mo, Zhaojun, 2023. Numerical simulation of a multi-stage magnetic refrigeration system in the temperature range of liquid hydrogen. Int. J. Hydrog. Energy.

Zimm, C.B., Ludeman, E.M., Severson, M.C., Henning, T.A., 1991. Materials for regenerative magnetic cooling spanning 20K to 80K. In: Advances in Cryogenic Engineering. Springer, pp. 883–890.